In vivo absorption, scattering, and physiologic properties of 58 malignant breast tumors determined by broadband diffuse optical spectroscopy

Albert Cerussi
Natasha Shah
University of California Irvine
Beckman Laser Institute
Laser Medical and Microbeam Program
1002 Health Sciences Road East
Irvine, California 92612

David Hsiang
University of California Irvine Medical Center
Chao Family Comprehensive Cancer Center
Division of Oncological Surgery
101 The City Drive
Orange, California 92868

Amanda Durkin
University of California Irvine
Beckman Laser Institute
Laser Medical and Microbeam Program
10020 Health Sciences Road East
Irvine, California 92612

John Butler
University of California Irvine Medical Center
Chao Family Comprehensive Cancer Center
Division of Oncological Surgery
101 The City Drive
Orange, California 92868

Bruce J. Tromberg
University of California Irvine
Beckman Laser Institute
Laser Medical and Microbeam Program
1002 Health Sciences Road East
Irvine, California 92612

Abstract. Diffuse optical imaging (DOI) may be a beneficial diagnostic method for women with mammographically dense breast tissue. In order to evaluate the utility of DOI, we are developing broadband diffuse optical spectroscopy (DOS) to characterize the functional origins of optical signals in breast cancer patients. Broadband DOS combines multifrequency intensity-modulated and continuous-wave near-infrared light to quantify tissue absorption and scattering spectra from 650 to 1000 nm. Values of intrinsic physiological properties (oxy- and deoxy-hemoglobin, water, lipid, and scatter power) derived from absorption and scattering spectra provide detailed information on breast physiology. We present the results of clinical studies of 58 stage II/III malignant breast tumors using a noninvasive, handheld, broadband DOS probe. On average, eight positions were scanned over tumor and contralateral normal breast for each subject. Intrinsic physiological properties were statistically significantly different for malignant vs. normal tissues for all subjects, without patient age or tumor size/type stratification. Breast tissues containing malignant tumors displayed reduced lipid content ($\sim$20%) and increased water, deoxy-, and oxy-hemoglobin ($>$50% each) compared to normal breast tissues. Functional perturbations by the tumor were significantly larger than functional variations in normal tissues. A tissue optical index (TOI) derived from intrinsic physiological properties yielded an average two-fold contrast difference between malignant tumors and intrinsic tissue properties. Our results demonstrate that intrinsic optical signals can be influenced by functional perturbations characteristic of malignant transformation; cellular metabolism, extracellular matrix composition, and angiogenesis. Our findings further underscore the importance of broadband measurements and patient age stratification in breast cancer DOI. © *2006 Society of Photo-Optical Instrumentation Engineers.* [DOI: 10.1117/1.2337546]

1 Introduction

1.1 Current Methods

The most effective screening technique presently employed for breast cancer is X-ray mammography; however, performance can be severely limited by high breast density.[1] Mammography has up to a 22% false negative rate in women under 50 years of age[2] and cannot accurately distinguish between benign and malignant tumors.[3,4] Sensitivity/specificity can range from 62.9%/89.1% in women with extremely dense breasts, to 87.0%/96.9% in women with almost entirely fatty breasts.[5] Digital mammography has shown similar overall diagnostic screening accuracy when compared to conventional film mammography, although some improvement over conventional film mammography has been observed in women under the age of 50.[6] Mammography has had favorable results when coupled with physical examination for monitoring the effectiveness of neoadjuvant chemotherapy.[7] However, the presence of fibrotic tissue,[7] high mammographic density,[8] remaining microcalcifications,[7,8] or ill-defined tumors,[9,10] makes response difficult to correlate with pathology or prognosis.[8,9,11–13]

Because of the variable performance of mammography in certain populations and settings, the use of optical methods as a supplement to present techniques for diagnosing and detecting breast cancer has generated considerable interest. Optical

Address all correspondence to Albert Cerussi, Beckman Laser Institute, University of California Irvine, 1002 Health Sciences Road East, Irvine, CA 92612 United States of America; Tel: 949-824-8838; Fax: 949-824-8413; E-mail: acerussi@uci.edu

methods are advantageous because they are noninvasive, are fast, are relatively inexpensive, and pose no risk of ionizing radiation. In order to establish a better basis for optical detection and diagnosis based on differential functional contrast, factors that affect the optical properties of both normal and tumor-containing breast tissue must be carefully examined and characterized.

Noninvasive frequency-domain photon migration (FDPM) methods have successfully detected the presence of small palpable breast lesions in women with previously diagnosed breast abnormalities.[14–18] FDPM methods have also been used to monitor the effectiveness of chemotherapy[19–22] and have been shown to correlate with measurements of mammographic density.[23] However, no clinical studies have been reported that characterize complete tumor NIR absorption and scattering spectra and physiological properties in a large population.

1.2 *Diffuse Optical Spectroscopy*

Diffuse optical spectroscopy (DOS) employs photon migration models and technology to probe a large sample volume, providing macroscopically averaged absorption and scattering properties at depths up to a few centimeters. The term "photon migration" refers to photons propagating diffusely throughout the tissue (i.e., in a random direction).[24] Quantitative DOS is based on time- or frequency-domain photon migration (FDPM) technology. In FDPM, near-infrared (NIR) light intensity modulated over a range of frequencies is used to characterize tissue in terms of optical parameters, i.e., the reduced scattering coefficient (μ_s') and absorption coefficient (μ_a).

The concentration of significant breast tissue light absorbers in the NIR (deoxy- and oxy-hemoglobin, water, and fat) can be calculated using the measured tissue μ_a.[25,26] Tissue scattering properties (μ_s') are believed to depend mostly upon intracellular structures such as nuclei[27,28] and mitochondria,[29] although extracellular components such as collagen also play a prominent role.[30–32] Cancer cells in suspension have been shown to differ in scattering from comparable normal cells.[33] Absorption and scattering together provide an understanding of changes in tissue composition and structure that are consistent with tumor growth. Factors such as total hemoglobin concentration (THb), tissue hemoglobin oxygen saturation (stO_2), and the spatial heterogeneity of the scattering parameter can serve as criteria for distinguishing between malignant and benign tissue.[17]

1.3 *Spectroscopy Enhances Optical Methods*

DOS instruments generally make use of only a few wavelengths and a limited number of source modulation frequencies. These instruments typically sacrifice spectral and modulation bandwidth for speed or imaging capability. We have developed a broadband DOS method based on a combination of multi-frequency intensity-modulated and continuous-wave spectroscopies to quantify thick tissue optical properties.[34] Our technical strategy uses the spectral scattering dependence and absolute absorption values obtained from discrete-wavelength multi-frequency FDPM measurements in order to translate broadband reflectance data into diffuse absorption and scattering spectra.[35] These NIR spectra provide insight into breast tissue composition and function.

NIR absorption spectra are sensitive to several important physiological components in breast tissue such as oxy-hemoglobin (ctO_2Hb), deoxy-hemoglobin (ctHHb), water (ctH2O), and lipids.*[30–32,36–41] Most optical mammography studies have focused upon the hemodynamic component of breast tissue, often ignoring or assuming water and lipid concentrations. Many of these studies have demonstrated that enormous hemodynamic contrast is available to NIR optical mammography.[15,18,23,42,43]

Oximetry measurements based upon discrete wavelengths can present problems in the recovery of hemodynamic parameters.[30,44–46] This is especially true in the breast, where the hemoglobin absorption is relatively small[30] and the compounding effect of water absorption plays a larger role.[44] Although it is possible to achieve accurate tissue hemoglobin saturation measurements with two optimized wavelengths, the choice of these wavelengths depends upon the optical properties of the tumor.[47] Algorithms may be used to optimize wavelength selection, or to spectrally weight component analyses, but without any *a priori* information it is prudent to have as many wavelengths as possible.

Although often ignored by the optics community, tissue water has received much attention in the MRI community. The apparent diffusion coefficient (ADC) of water is a measure of the diffusion of bulk water in tissues. The ADC of water has been found to correlate with cellular density (or cellularity) in several tissues, including brain,[48–51] breast,[52–54] and bone marrow.[55,56] Detailed studies using human melanoma xenografts[57] and breast tumor animal models[58] have supported these findings. The ADC of water has also been found to relate to cellular pathology.[56,59] Most relevant to our discussion are the ADC of water differences displayed by benign and malignant breast lesions.[52,53] The ADC of water is lower in malignant lesions relative to normal tissues because the higher cellularities in malignant tissues often slow down the diffusion of water. Thus, the ADC of water, and perhaps the corresponding increases in water concentration, can provide a link to the cellular microscopic environment.

Lipids also play a role in optical mammography. Co-registered measurements of optical and MRI data in homogeneous tissue phantoms have shown both techniques measure lipid and water concentrations with high accuracy.[60] In some cases, a breast may be viewed in the simplest fashion as a layer of lipids surrounding a layer of glandular tissue. However, this is not always true, and breast lipids strongly change with age and, in particular, menopausal status. The effects of lipids, especially as a layer, can dramatically influence efforts for quantitative image reconstruction if ignored.[61] Benign lesions such as lipomas and perhaps cysts can be identified by the lipid content.[40]

1.4 *Project Goal*

The goal of this study was to identify the NIR functional contrast between normal breast tissue and breast tissue with malignant tumors within a small but statistically relevant population of subjects. We define contrast in this contribution as the difference between malignant and normal tissues. The

---

*Our notation is designed to comply with the suggestions of Zander and Mertzlufft: the "c" denotes a concentration (μM), the "t" denotes the tissue, and the T denotes the total.
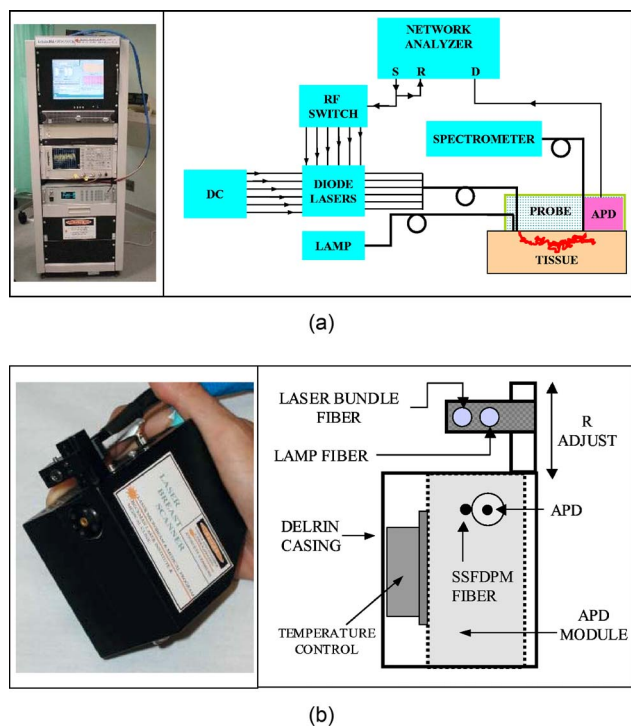
Fig. 1 Instrument diagram. The current cart-based clinical system combines a six-wavelength frequency-domain instrument (660–850 nm) with a broadband steady-state spectrometer system (650–1000 nm) depicted in panel (a). The handheld probe, which is placed upon the breast tissue region of interest, is diagrammed in panel (b). "S" is the RF source, "R" is the RF reference, and "D" is the RF detection channel.

rich spectral content in these studies clearly demonstrates the clinical potential of quantitative NIR tissue spectroscopy. In addition, we expect that this information will be useful for identifying regions of optimal spectral contrast in the development of optical tomographic and imaging techniques.

2 Methods

2.1 Absorption Spectroscopy in Diffusive Media

The intense multiple scattering nature of tissues greatly increases the photon path length, which complicates measurements of tissue absorption coefficients. The photon path has been shown to vary considerably in many tissues and is thus not usually known *a priori*. We have employed FDPM theory in order to separate the effects of absorption and scattering in tissues. The technical aspects of this theory have been discussed in the literature.[62,63] Specifically, we have used a P_1 approximation to the transport equation in the semi-infinite geometry using an extrapolated boundary condition.[64,65]

2.2 Instrumentation

The specific details of broadband DOS have been described elsewhere.[35,66] Briefly, the instrument is comprised of two key components: a 6 wavelength frequency-domain component and a broadband steady-state component (Fig. 1(a)).

The FDPM instrument currently employs six commercially available laser diodes (661, 686, 786, 808, 822, and 852 nm); older versions of this instrument included additional laser di-

odes at 911, 956, and 973 nm. Each laser diode is amplitude modulated serially between 50 to 500 MHz in steps less than 2 MHz by combining a DC bias current and RF modulation current provided by a conventional network analyzer. A 3-mm fiber bundle, composed of six 400-micron-diameter fibers, delivers the laser light to the subject. Each laser delivers less than 20 mW of optical power to the tissue.

A hand-held probe houses an avalanche photodiode detector (APD) that records modulated diffuse light signals after propagating through the tissue (Fig. 1(b)). The particular APD we have used (<1 mm^2 active area, 600 MHz 3 dB cutoff point) is housed inside a sealed module. This hand-held probe has a plastic attachment on the casing to position source optical fibers at variable distances from the APD. The network analyzer acts as a fast electronic heterodyning digitizer by comparing a small fraction of the source electronic signal with the electronic signals generated by the APD. Thus, the phase and amplitude of the detected diffusive optical signals are measured as a function of source modulation frequency. The total FDPM measurement time is approximately 20 s. However, the actual sweep and acquisition time is actually only 200 ms per wavelength.

It is not possible to implement hundreds of laser diodes to cover the entire NIR spectral region. Additionally, we have found by experience that the source modulation depth of laser diodes higher than 900 nm tends to be much lower than for laser diodes between 600–850 nm. This lower modulation depth decreases the measurement signal to noise, particularly at higher modulation frequencies. To increase the spectral bandwidth, we have integrated a steady-state (SS) spectrometer system into our instrument.[35] The integrated SS system interpolates and extrapolates values of μ_a in regions where laser diodes are not commercially available. In addition, we have found this combined technique does not require laser diodes beyond 900 nm. However, the SS spectra must be acquired alongside the FDPM information in order to produce absolute quantitative absorption spectra, for reasons that are described ahead.

2.3 Fitting Considerations

FDPM instrumentation artifacts such as cable length and source strength variability introduce additional unwanted phase shifts and amplitude decreases. These artifacts were removed by calibrating the measured photon density wave phase and amplitude with the phase and amplitude of light detected in a tissue-simulating phantom with known optical properties.[66] A standard integrating sphere was also used to remove wavelength-dependent artifacts from the SS source, spectrometer, and optical fibers.

By fitting instrument-corrected data to a P_1 approximation to the radiative transport equation, we can recover μ_a independently from μ_s' for the tissue. We typically fit data from 50 to 500 MHz while keeping the source detector separation fixed in order to recover μ_a and μ_s'; thus, only a single distance is needed for optical property measurements. A Levenberg–Marquardt minimization algorithm was adapted to fit simultaneously both the real and imaginary parts of the signal (i.e., phase and amplitude) by minimizing a χ^2 merit function. Several initial guesses were used to verify that the minimum χ^2 was not strictly a local minimum. This FDPM fit

was accomplished using the 'lsqcurvefit' routine in MAT-LAB™. The end result is a discrete spectrum of μ_a and μ_s' values at each of the laser diode wavelengths.

SS broadband spectra were converted into absolute absorption spectra using two simple steps. First, the spectral shape of the reduced scattering is assumed to follow a power law[67,68] of the form $\mu_s' = A\lambda^{-sp}$, where A is the scatter amplitude and sp is the scatter power, or the exponent of the scattering spectrum. The power-law fit to the FDPM discrete laser diode spectrum provides a scatter correction of the SS reflectance spectrum. Second, we fit the SS intensity at each of the laser diode wavelengths to the FDPM-measured absolute absorption values. Thus, the SS reflectance spectrum intensity is scaled using the FDPM discrete laser diode measurements. The absolute absorption spectrum is then extracted by fitting the corrected reflectance spectrum to a diffusion model[69] using the 'fzero' function of MATLAB™.

In a typical measurement, we measured the tissue twice, and then measured the phantom several times. This procedure provided precision errors that emerged from coupling variability between the probe to the phantom and from the probe to the tissue. The biggest variation in our measurements was due to the variability in coupling to the phantom.

2.4 Spectral Processing

Complete details of the processing of typical DOS data have been described.[30,34] The absorption spectrum provides the information needed to solve a weighted, nonzero, least-squares problem (using 'lsqlin' in MATLAB™) to recover the concentrations of the principal NIR absorbers. No *a priori* knowledge about these chromophore concentrations has been assumed (other than standard non-negative constraints). Each matrix is overconstrained because we measure many more wavelengths than chromophores. We assumed that the only chromophores were H_2O, lipids, O_2Hb, and HHb. Molar extinction values for water were obtained from Kou et al.[70] Molar extinction values for lipids (soybean oil) were obtained from Eker.[71] Oxy and deoxy hemoglobin molar extinction coefficients were obtained from Zjilstra et al.[72] Other NIR chromophores such as myoglobin and cytochromes were assumed negligible in breast tissue and therefore ignored.

2.5 In Vivo Measurements

A series of broadband DOS measurements were taken on a population of 58 malignant breast tumors in 57 subjects. General patient information may be found in Table 1. The mean subject age was 50.5 (13.8) with a range of 18 to 81. The mean body-mass index (BMI) was 27.5 (7.1), with a range of 18.8 to 47.8. Linear reflectance linescans were performed in all subjects both over the region of the tumor and in the same location on the contra-lateral side (Fig. 2). The linescan location was chosen based upon *a priori* knowledge of the tumor location from standard X-ray mammography; thus, the intent of this data was not to screen for suspicious lesions but to characterize malignant lesion optical properties. We assumed that the contralateral side was normal tissue unless otherwise indicated in the final pathology report. For mastectomy patients ($N=3$) we used the opposite side of the same breast as the normal tissue region, unless otherwise indicated in the pathology report.

**Table 1** General statistics of the patient population.

Item	Value
Subjects (#)	57
Mastectomies (#)	3
Age (years)	50.5 ± 13.8
BMI (m^2/kg)	27.5 ± 7.1
# Points, normal side	8 ± 2
# Points, tumor side	9 ± 3

Linescans were generally performed in 10-mm steps (a few were 5 mm) using a source–detector separation of 28 mm. Measurements were repeated twice to evaluate placement errors at each grid location. Characteristics of the tumors studied in this paper are presented in Table 2. The average tumor size, which was taken to be the maximum tumor dimension, was 27 ± 21 mm, with a range of 5 to 113 mm (reported for 55 of 58 tumors). The average Bloom–Richardson score was 6.2 ± 1.5, with a range of 3 to 9 (reported for 37 of 58 tumors). All tumor classifications were evaluated by standard clinical pathology.

2.6 Linescan Geometry Characterization

Given the diffusive nature of light, tumor linescans can be convolved with regions of normal tissue. In our reflectance geometry, the fraction of tumor to normal tissue depends upon the location of the lesion along the linescan axis and the lesion depth. We considered various simple means for characterizing the optical and physiological properties of linescans, as depicted by an arbitrary DOS parameter in Fig. 3. First, we calculated the average value of the parameter for all linescan locations (T_{AVG}), as indicated by the dotted line. We then determined the parameter maximum value, which is denoted by the term T_{MAX}. This linescan location was assumed to be the best single location that represented tumor tissue. In order to represent a larger volume of tissue, we defined a value T_{PEAK}, as shown by the angled dotted ellipse, which is defined as the average parameter at the three highest continuous points in the linescan, one of which was T_{MAX}. Finally, we located the lowest continuous parameter value on the tumor linescan, which was usually the farthest away from T_{PEAK}, and averaged them to obtain a tumor-side normal baseline (T_{BASE}). As for the contralateral normal side, we always report the average of the linescan (N_{AVG}).

In order to locate the lesion, we used a previously proposed contrast function known as the Tissue Optical Index (TOI).[39] Since in general, we have found that tumors possess higher concentrations of water and total hemoglobin, lower lipids and stO_2, we decided upon the following original function:
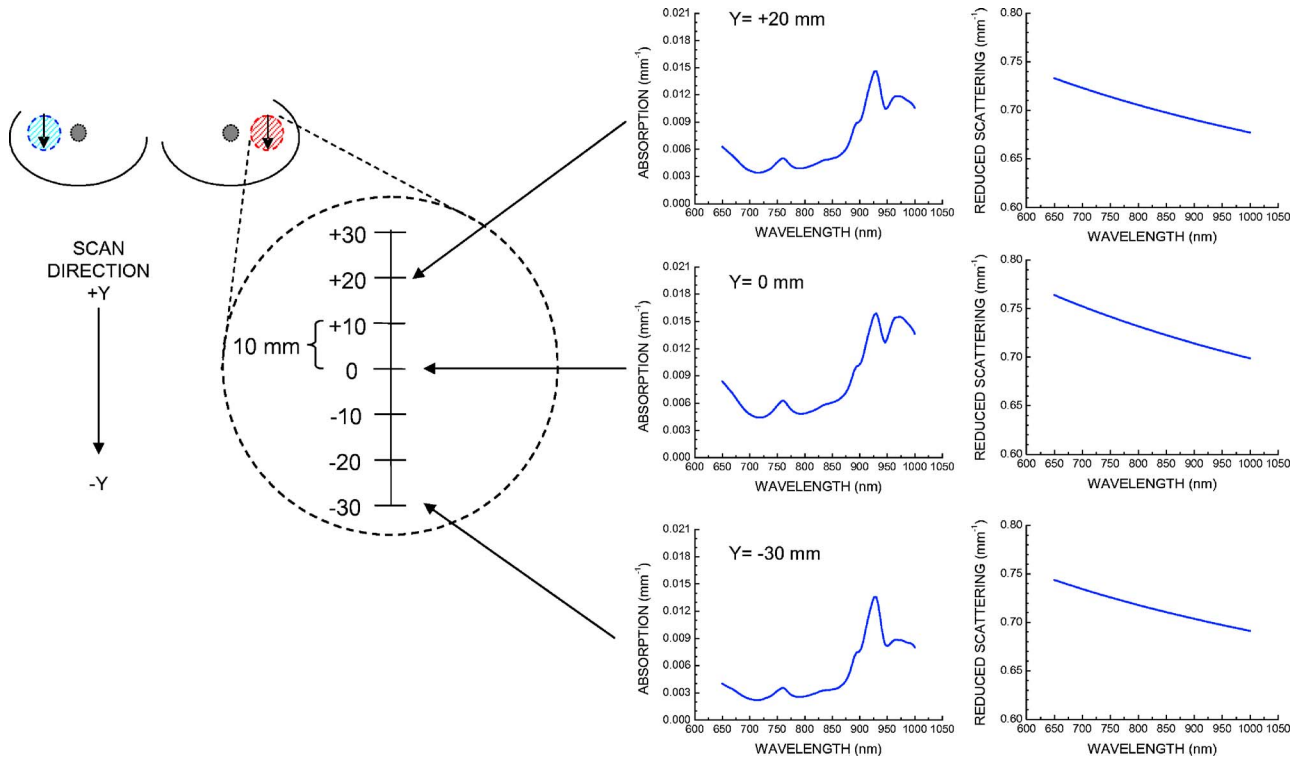
Fig. 2 Linescan geometry. The handheld probe was moved along a linear grid of steps spaced 10 mm apart. Each point of the linescans was measured twice (the resulting fitted spectra are shown). Both the tumor region (which had been previously identified) as well as the contralateral normal side was measured. In the event of mastectomy, the opposite side of the same breast was scanned. Note that the orientation, location, and number of points of the linescan varied with the clinical presentation of the lesion.

$$TOI = \frac{ct\mathrm{H_2O} \times ctTHb}{\mathrm{LIPID} \times st\mathrm{O_2}} \quad \text{(original)} \qquad (1)$$

Thus, the location of T_{MAX}, unless otherwise noted, is taken to refer to the point on the linescan where TOI is a maximum. All tumors in this study displayed contrast differences in this TOI parameter between the tumor linescan and the normal issue linescan.

However, as we detail in Sect. 4, we have observed in this statistical study that the $st\mathrm{O_2}$ is not as sensitive as the base DOS parameters such as $ctHHb$ and $ct\mathrm{H_2O}$. Additionally, we also desire an index that is itself not a function of other indices (namely, $ctTHb$ and $st\mathrm{O_2}$). For these reasons, we have elected to represent the hemodynamic contribution to this index by hemoglobin parameter, $ctHHb$. Thus, the updated index becomes

$$TOI = \frac{ct\mathrm{H_2O}}{\mathrm{LIPID}} \times ctHHb \quad \text{(modified)} \qquad (2)$$

For the purposes of this study, we have found that both the revised and original TOI functions report similar results in terms of spatial location of maximum lesion contrast with respect to a normal tissue baseline. The updated TOI, however, generally reports higher relative contrast.

2.7 Statistical Considerations

Nonparametric statistics were used for all statistical tests to remain free of normality assumptions. Comparisons between tissue regions were performed using two-tailed Wilcoxon/ Kruskal–Wallis Rank Sums tests. Significance was assumed at a confidence interval of 95% ($\alpha=0.05$) for a two-tailed dis-

Table 2 General population statistics of the patient tumors.

Item	Value	SD	MIN	MAX	MEDIAN
Maximum tumor dimension (mm)	27	21	5	113	23.5
BR score	6.2	1.5	3	9	6
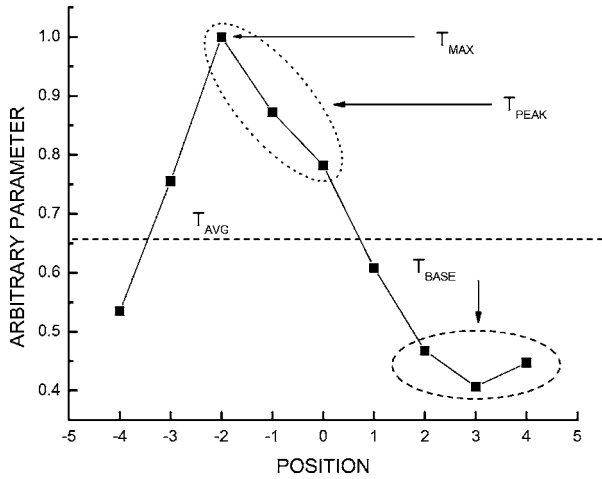
Fig. 3 Tumor linescan characterization. Definitions used in characterizing tumor linescans for an arbitrary linescan parameter. Note that these definitions do not account for the tumor depth or orientation.

tribution. We further assumed that all measurements were independent. All statistical calculations were performed using commercial software (JMP IN; SAS Institute, North Carolina). Error bars for population data are the standard deviation of the population (i.e., not the standard error of the mean).

2.8 *Study Limitations*

The purpose of this study was to determine the diffusive optical signatures of malignant lesions in breast tissue. In all cases, tumor general locations were known *a priori*, as denoted by standard X-ray mammography. Thus, our results should not be interpreted as the findings of a screening study. Data were not stratified into classification categories beyond malignant and normal.

Another limitation is that we did not consider benign lesions in this study. Differentiation between malignant and benign tumors is a challenging diagnostic problem. We did not have enough benign lesion statistics to make meaningful comparisons and thus they were not included in this study. In the interest of simplicity we felt it was best to relegate our analysis to malignant lesions. A study comparing the signatures of malignant and benign lesions is forthcoming.

The third limitation of this study is that depth information was not always available. All tumors were identified via standard mammography, but modalities that typically report depth (such as MRI and ultrasound) were not routinely available. Thus, the actual values of tumor versus normal will be skewed with the depth. Nevertheless, this dataset reports the nature of the contrast available.

Five subjects who fit the criteria described in this report were measured but not included in this analysis. One patient measurement was discarded because of technical problems during the control measurement on normal breast tissue. Another subject was excluded because of un-physical lipid and water values (i.e., beyond 100%), which may be the result of excessive tumor edema or improper calibration. In another subject, the tumor signature was identified, but the control side displayed one point of unusually high TOI contrast (comparable to the tumor) that could not be explained. In the two
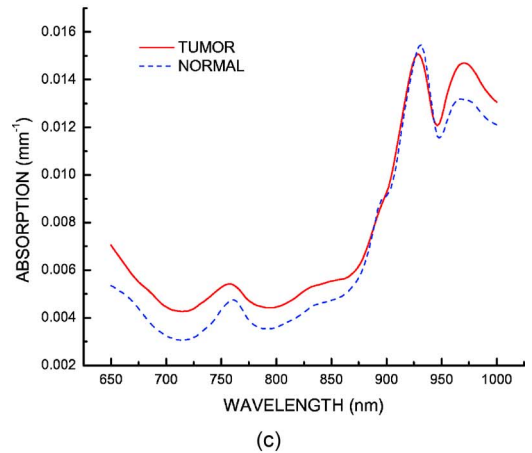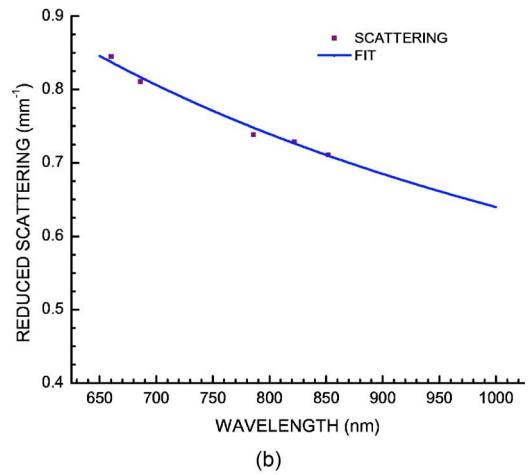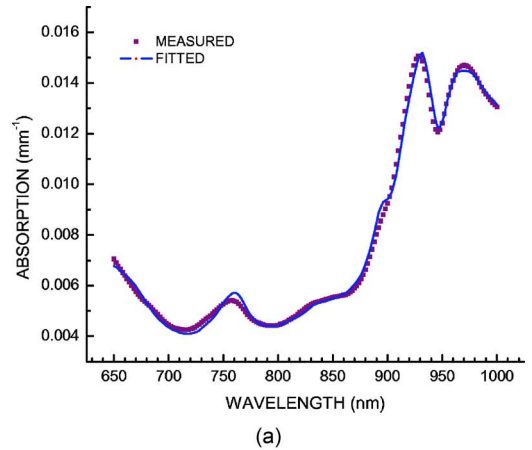
Fig. 4 Typical tumor spectra. A closer look at typical (a) absorption and (b) reduced scattering spectra from breast tissue in a single subject. The absorption fit (solid line) is the result of a positive-constrained least-squares fit, assuming a basis set of HHb, O_2Hb, H_2O, and lipids. A power law fit ($\mu_s' = A\lambda^{-SP}$), represented also by a solid line, was applied to the reduced scattering data in (b). Notice how the absorption spectra between tumor (at the linescan TOI peak) and normal differ in plot (c) where the dotted curve represents the spectrum measured in the same region of tissue on the contralateral (normal) breast.
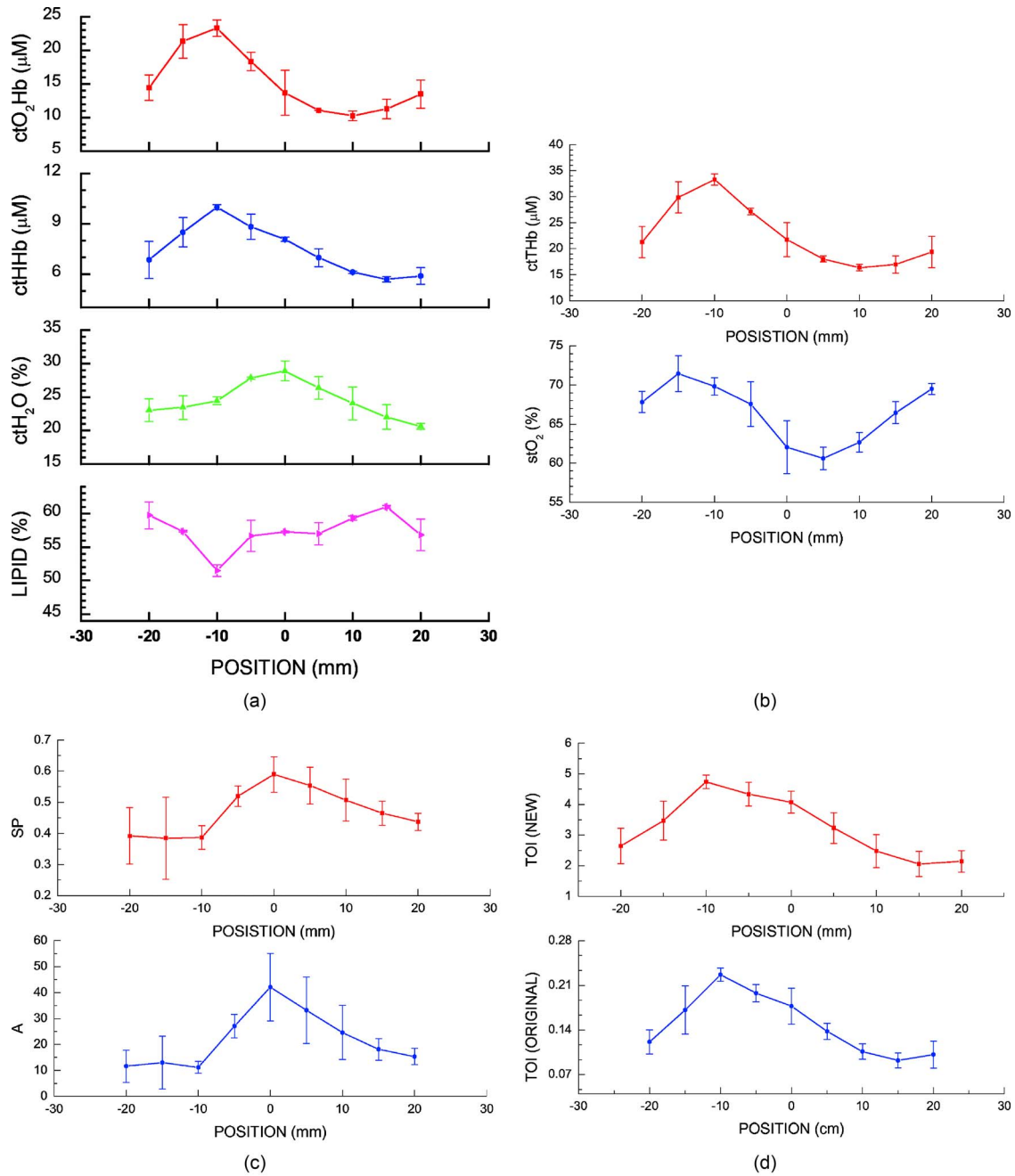
Fig. 5 Typical tumor linescans. DOS linescans from a $10 \times 15 \times 10$-cm lobular carcinoma *in situ*. Panel (a) demonstrates the changes as functions of position in the four basis absorption components. Panel (b) presents the hemoglobin contrast functions ctTHb and stO$_2$ for the linescan. Panel (c) presents the scattering information as represented by the prefactor and scatter power according to a power law description with μ_s' in mm^{-1}, and λ in μm. Note carefully that the parameters do not all peak/trough at the same location. Panel (d) provides a summary by displaying the TOI, both old and updated, for these linescan data. Error bars represent the differences between the two linescans.

remaining subjects, no TOI contrast was detected, presumably because the lesion location was not properly identified or the lesion was too deep for our source–detector separation to probe adequately.

3 Results

3.1 Basic Characteristics of Tumor Spectra

How do tumor spectra differ from normal tissue spectra? Figure 4(a) provides typical spectra from a malignant tumor in the breast of a 51-year-old female subject with a $2.3 \times 1.6 \times 1.9$ cm adenocarcinoma. Panel (a) presents the measured μ_a spectrum from 650 to 1000 nm in a region of tumor-containing tissue. There are several prominent spectral features displayed. There is a large peak in the 930-nm region that is characteristic of lipids, which are plentiful in normal (and especially postmenopausal[30,32] breast. There is also a prominent peak in the 970-nm region that is characteristic of a high water concentration.[19,30,40,73] Typically this water value

Table 3 Results of normal average linescan vs. tumor average linescan.

Parameter	N_{AVG}		T_{AVG}		P
Name	Mean	Median	Mean	Median	Wilcoxon
ctHHb (μM)	5.10±1.7	4.8	7.53±2.8	6.74	<0.0001[a]
ctO$_2$Hb (μM)	12.4±6.2	10.7	17.2±7.5	15.4	0.0004[a]
LIPID (%)	66.1±10.3	66.0	58.5±14.8	61.7	0.008[a]
ctH$_2$O (%)	18.7±10.3	15.0	25.9±13.5	23.3	0.0007[a]
SP	0.579±0.231	0.538	0.725±0.319	0.658	0.024[a]
LN(A)[b]	4.0±2.0	3.53	5.2±2.6	4.49	0.022[a]
stO$_2$ (%)	67.7±9.3	69.3	67.5±8.4	69.4	0.72
ctTHb (μM)	17.5±7.5	15.6	24.7±9.8	22.5	<0.0001[a]
LN(TOI)[b]	2.68±1.3	2.62	3.82±1.6	3.55	0.0013[a]

[a]Indicates significant result.
[b]Natural logarithm of parameter.

is lower in normal postmenopausal breast tissue.[30,32] The peak near 760 nm is a well-known spectral characteristic of deoxyhemoglobin. Normal breast tissue, particularly in postmenopausal women, contains very little hemoglobin compared to other tissues such as muscle and brain.[30,31,74,75] Overall, the absorption begins to increase in the red part of the spectrum, especially in the 600-nm region where hemoglobin absorption becomes very large. The solid line in Fig. 4(a) is a fit of the four-component basis spectra (HHb, O$_2$Hb, H$_2$O, lipid) to the measured μ_a.

Figure 4(b) presents the measurement of the reduced scattering in tumor-containing tissue in the same patient. The six points represent the FDPM-measured μ_s' values, and the line represents the nonlinear power law fit to these data. In general, we have found that both scatter amplitude and scatter power were strongly correlated.

Figure 4(c) is a comparison between the absorption spectra of tumor-containing breast tissue (the same spectrum as above in Fig. 4(a)) and the absorption spectra from the same location on the contralateral side (i.e., presumed normal, dotted line). Immediately we can see characteristics that differ between the tumor and normal spectra. The tumor region contains higher levels of water and reduced levels of lipid, as evidenced by increased absorption at ~970 nm and decreased absorption at ~930 nm, respectively. A significant increase in tumor hemoglobin is indicated by changes in absorption between 650 and 850 nm. By applying the results of the four-component basis spectra fit we can generate quantitative concentrations for the components.

3.2 Basic Linescan Characteristics of Tissue Properties

How do these calculated DOS-measured parameters vary spatially across the linescan? Figure 5 provides the calculated concentrations plotted as functions of linescan position for a $10 \times 15 \times 10$ mm tumor in the breast of a 39-year-old sub-

ject. Points on this grid are separated by 5 mm, as indicated in the figure. Error bars represent differences between the two linescans (~10%). The lesion was an infiltrating ductal carcinoma, with less than 10 mm diameter along the largest axis. We observe in Fig. 5(a) an increase in tissue hemoglobin near the −10-mm location, both in oxy and deoxy forms. These values are to be compared with the tissue baseline, which for our purposes is located at positions +15 & +20 (20–30 mm away). There also exists a strong peak in the water concentration, but at the center of the linescan. A trough exists in the lipid fraction at the −10-mm location. Figure 5(b) continues by demonstrating a peak in ctTHb at the −10-mm location, but a trough in the stO$_2$ at the +5-mm location. The scatter power expresses a peak at the center of the linescan (as does the water), but note that the lowest portion of the linescan exists in the −10-mm position in Fig. 5(c). That all parameters do not peak or trough at the same spatial location is noted.

We can assemble multiple functional parameters from Fig. 5(a) into a single index to enhance the differences between normal and tumor. Figure 5(d) provides two such indices. The bottom curve (circles) is a plot of the original TOI parameter [Eq. (1)], which demonstrates a maximum at the −10-mm location and a peak-to-baseline contrast ratio (T_{MAX}/T_{BASE}) of about 2. The top curve (squares) represents the newer TOI index [Eq. (2)], which demonstrates a maximum at the same location.

3.3 Population Statistics: Average Values

Are these DOS-measured differences preserved over a larger population? To test this hypothesis, we performed comparisons of all measured and calculated parameters for the entire population of 58 malignant tumors. Table 3 provides the results of comparisons between the tumor and contralateral normal linescan averages (T_{AVG} and N_{AVG}, respectively). For each linescan we calculated both the mean and the median

Table 4 Contrast of tumor relative to normal tissue variations.

Parameter Name	ΔT		$\Delta T / N_{SD}$	
	Mean	Median	Mean	Median
ctHHb (μM)	4.62	3.7	7.30	5.65
ctO$_2$Hb (μM)	7.90	5.84	3.53	2.51
LIPID (%)	−14.1	−10.7	−3.61	−3.17
ctH$_2$O (%)	13.3	9.08	8.18	4.12
SP	0.198	0.130	1.88	1.24

(a)

(b)

Fig. 6 Composite of all tumor absorption spectra. Panel (a) provides the averages for all T_{MAX} and T_{BASE} absorption spectra for the 58 tumors patients in the study. We have stratified the T_{MAX} spectra them according to an age-dependent breakdown as discussed in the text. Note the clear changes between pre- and post-menopause, particularly in the 900-nm and above spectral region. Panel (b) groups the spectra into three age categories: A (under 40), B (40–50), and C (over 50). Note each age category generally represents pre-menopause, peri-menopause, and post-menopause for categories, A, B, and C, respectively.
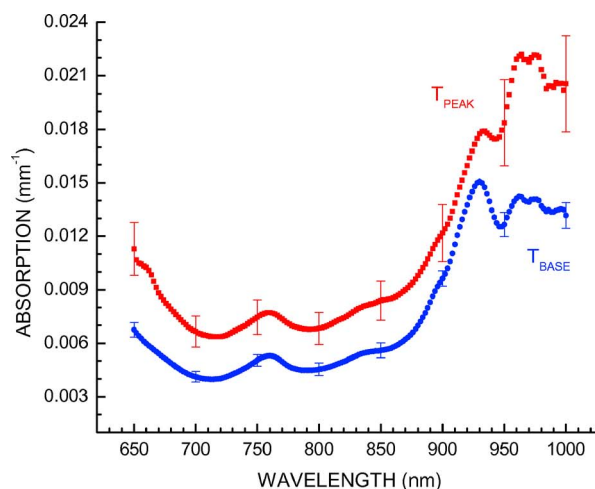
value. We performed nonparametric standard tests for significance for these values (Wilcoxon Ranked-sum test). The results of the analysis show that the basis chromophores, HHb, O$_2$Hb, H$_2$O, and lipids, all display statistically significant differences between normal and malignant tumor-containing tissue, as demonstrated via the spectra in the previous figures. Significance was achieved at the 95% confidence interval using a two-tailed distribution. In particular, the variance in A was quite large, mostly due to some very extreme values. So as to not skew the average, we instead report the natural logarithm of the values, noting that statistical significance was still observed with the nonparametric test.

As for calculated indices, the ctTHb displayed statistical significance while the stO$_2$ did not. Thus, the inclusion of stO$_2$ in the TOI may not be justified in every case. As described by Eq. (2), we replaced the ratio of ctTHb/stO$_2$ with the most sensitive hemodynamic parameter, ctHHb. Table 3 demonstrates that differences between N_{AVG} and T_{AVG} differ in statistically significant fashion according to the two-tailed Wilcoxon Ranked-sum test ($Z = 0.0013$). Note that the data presented are the natural logarithm of the TOI since the range of TOI values is quite high. The contrast ratio between N_{AVG} and T_{AVG} in TOI was the highest amongst all the parameters ($\sim$ factor of 3).
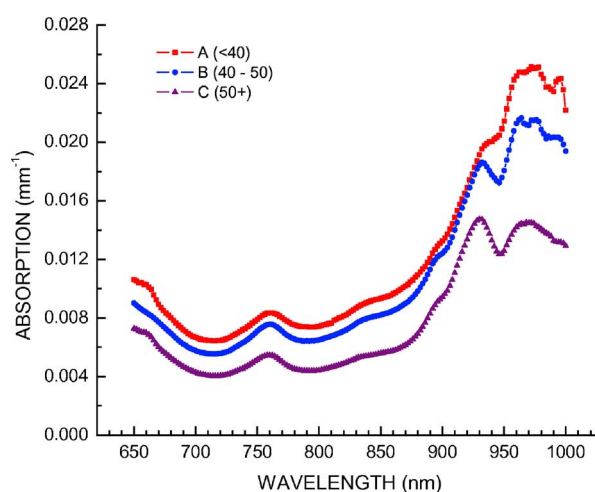
3.4 Population Statistics: Tissue Variations vs. Tumor Perturbations

The average linescans in effect average out the differences between tumor and normal because the tumor linescan includes several points far from the lesion site. But how do the tumor features compare relative to the intrinsic physiological variations of normal tissue? Table 4 provides the average and median contrast difference in DOS base parameters for the tumor with respect to the background, which is defined as $\Delta T = T_{MAX} - T_{BASE}$ for all 58 subjects. In addition, we compare the ΔT with the standard deviation of the contralateral normal breast (N_{SD}) for each DOS parameter. A value of unity implies that the physiological perturbation by the tumor is on average the same as the intrinsic physiological variation in normal tissues.

The results are in general the same as for the tumor averages, but we can now understand these variations as a physiological signal-to-noise. The strongest average relative contrast belongs to ctH$_2$O ($\sim$8.2) and ctHHb ($\sim$7.3), followed by lipids and ctO$_2$Hb ($\sim$3.5 each) and then finally by the SP

(<2). We note that the lipid difference is negative because lipids tend to decrease in the presence of a tumor. We confirmed that ΔT was significantly different than the NSD for all DOS base parameters (Wilcoxon, $p < 0.0001$).

3.5 Age-Related Absorption Spectra Comparison

We plot the average T_{MAX} spectrum against the corresponding average T_{BASE} spectrum in Fig. 6(a). Error bars represent the standard error in this case and are plotted only every 50 nm for clarity. The general features of the previous analysis are demonstrated here, such as higher absorption in the hemodynamic range and especially higher water absorption. We note that there is considerable variation amongst the T_{PEAK} spectra,

Table 5 Tumor functional properties stratified by patient age.

Category	ΔctHHb (μM)	ΔctO$_2$Hb (μM)	ΔctH$_2$O (abs %)	ΔLIPID (abs %)	ΔSP
<40	8.1±1.2	13.8±2.3	27±4	−24±3	−0.34±0.11
40 to 50	2.5±1.3	5.7±1.7	11.4±3.4	−13±3	−0.17±0.06
>50	3.5±1.0	5.6±1.2	6.9±1.2	−9.7±2.2	−0.13±0.03

and less variation amongst the $T_{\rm BASE}$ spectra. It is noteworthy that although statistically we observe differences between the spectra, the measured spectra also exhibit some degree of overlap. For example, there are normal subjects who display ctHHb values that are higher than other subjects with tumors.

We can gain some insight into this effect by plotting each of the $T_{\rm MAX}$ spectra for three age groups in Fig. 6(b): <40(N=16), 40 to 50 (N=10), and >50 (N=32), We note that the average spectrum appears age-dependent. As subjects age, with a menopausal transition at about 51 years, we can see the clear differences in tumor spectra between younger and older women.

The differences between younger and older women can be quantified by averaging the fitted components according to age category. Table 5 provides within each age category the average of the difference between $T_{\rm MAX}$ and $T_{\rm BASE}$, where errors here are again the standard error of the mean. While it is clear that there are differences in baseline functional properties between ages, we observe that the differences between $T_{\rm MAX}$ and $T_{\rm BASE}$ are age-dependent. In addition, we note that the differences between $T_{\rm MAX}$ and $T_{\rm BASE}$ (i.e., tumor contrast) are greatest in the spectral features above 900 nm (ctH$_2$O and Lipids). Nonparametric Kruskal–Wallis tests with the Bonferroni correction (where p=0.05/3=0.017 implies significance) confirm that the age categories are not representative of the same population, with significance probabilities of 0.001 for ctHHb, 0.002 for ctO$_2$Hb, <0.001 for ctH$_2$O, and 0.002 for lipids.

3.6 Scattering Spectra

We have also plotted for all 58 subjects the fitted scatter amplitude versus the fitted scatter power for three classes of measurements: $N_{\rm AVG}$, $T_{\rm BASE}$, and $T_{\rm MAX}$ in Fig. 7. In each case, there is a high degree of coupling between the scatter amplitude and scatter power. The lines are semi-log fits to these data for each measurement class. The slopes of the lines are 3.57±0.15 (r=0.95, p<0.0001), 3.23±0.10 (r=0.97, p<0.0001), and 2.90±0.08 (r=0.98, p<0.0001) for $N_{\rm AVG}$, $T_{\rm BASE}$, and $T_{\rm MAX}$, respectively. The power-law fit comprises six wavelengths ranging from 660 to 850 nm.

Using nonparametric statistics as before, we verified that the A to SP ratio changed significantly between $N_{\rm AVG}$ and $T_{\rm MAX}$ (p=0.01). Likewise, the A and SP ratio changed significantly between $T_{\rm BASE}$ and $T_{\rm MAX}$ (p=0.02). In contrast, the A and SP ratio was not found to be significantly different between $T_{\rm BASE}$ and $N_{\rm AVG}$ (p=0.97). For this reason, a three-way comparison (Kruskal–Wallis) between the A to SP ratio at each of the three measurement locations was not found to

be significant (p=0.02) after adjusting the significance level using the Bonferroni correction for multiple comparisons.

3.7 Effect of Tumor Size

Although this was not an imaging study, we report the effect of tumor size on the linescan measurements. The maximum tumor size was chosen because it was the most consistently reported measure of tumor size. Our analysis also does not take into account the actual tumor orientation. We did not observe any correlation between the maximum tumor size and the tumor peak values (Fig. 8) for each of the base absorption-derived DOS parameters. The maximum tumor size was determined from the pathological and radiological findings. There will be of course some discrepancy between pathological and radiological distances but not enough to change the results of these findings. Note that this lack of correlation does not imply this will be true for all measurements, but in our nondepth sectioned study we did not see this correlation.

There is, however, a weak correlation between the spatial extent of DOS linescans and the tumor size. The normalized area of the linescan was determined by (a) calculating the difference between TOI $T_{\rm PEAK}$ and $T_{\rm BASE}$ over the linescan, and (b) scaling the result between 0 and 1. In this way, non-tumor linescan locations contribute zero whereas the maximum contributes a value of 1. By normalizing the data, we have removed all age-dependent effects and focused solely on
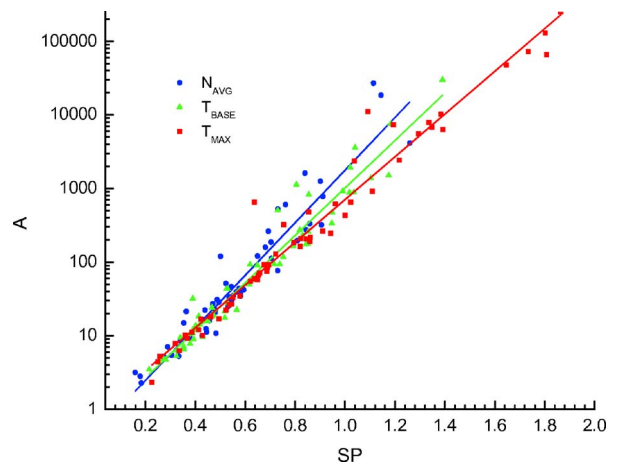
Fig. 7 Plot of scatter amplitude versus scatter power for $N_{\rm AVG}$, $T_{\rm BASE}$, and $T_{\rm MAX}$. The scattering amplitude and power are correlated. The scatter amplitude and scatter power were determined from a nonlinear fit of six wavelengths (650–850 nm). The slopes of the lines are provided in the text and are clearly different.
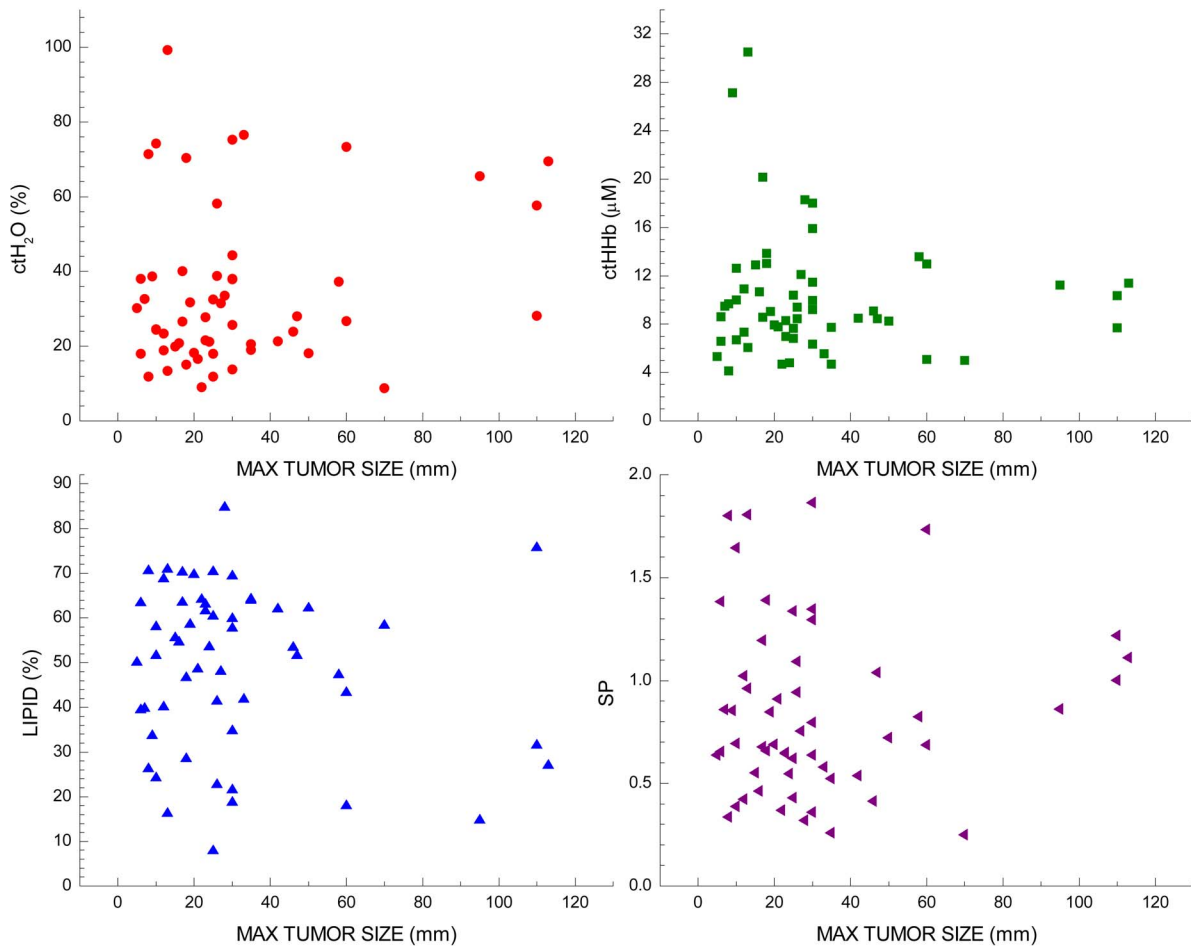
Fig. 8 Plots of DOS basis parameters versus the largest size dimension of the tumor. No correlations between the tumor maximum size and the DOS spectroscopic parameters were found.

the spatial characteristics of the linescans. Table 6 outlines a breakdown of 46 lesions in terms of size. We included only 46 of the 58 lesions because (a) 3 lesion sizes were not reported in the radiological or pathological reports, and (b) 9 linescans did not cover the entire lesion, and thus the area calculation would not faithfully represent the tumor volume. In general, the size categories were chosen to reflect similar numbers of counts, using as small of a distance range as possible; note that the last few categories, for which there are less counts, have wider size intervals. The size reported in this case is the maximum lesion dimension.

Figure 9 provides plots of ctH_2O, ctHHb, and ctTHb, and TOI versus the lesion size category. The error bars represent the standard deviation of all lesions that lie within each lesion size category. Although the variation is substantial, a general linear trend can be observed for all DOS-measured parameters. Of the fits, only ctH_2O (0.21 ± 0.14, $p=0.0009$) and ctHHb (0.17 ± 0.14, $p=0.0007$) display a slope that is clearly greater than zero despite the errors.

3.8 Effect of Tumor Pathology

Is there a link between the macroscopically measured optical properties and the histological character of the tumor? Figure 10 plots the T_{MAX}-value of ctH_2O versus the Bloom–Richardson score.[76] The Bloom–Richardson score, as updated by Scarff (SBR), is a histological grading scale ranging from 3 to 9, that accounts for tubule formation, nuclear pleomorphism, and mitosis counts.[77] The SBR score was determined by pathologists, but only reported for 37 of the 58 tumors. Each SBR level for the lower categories is generally underrepresented with only $N=2$ for a score of 3 and $N=1$ for a score of 4. Error bars represent the average ctH_2O value for each SBR score. Although the variation is high, a general pattern exists. The SBR score increases with increasing ctH_2O with a high degree of linearity ($R=+0.98$). The solid line represents an error-weighted fit to the data points; however, we excluded the SBR=4 points because $N=1$ did not allow for error bars. The slope of the line was 4.36 ± 0.58 ($p=0.0004$) and the intercept was 5.8 ± 3.8. We also checked the N_{AVG}-value of ctH_2O on the contralateral normal breast against the SBR score of the tumor. However, as expected, we failed to see any correlation ($R^2=0.07$), with an effective slope near zero (-0.45 ± 0.86, $p=0.62$).

ctH_2O displayed the most significant correlation with SBR. The same general effect was observed for ctO_2Hb ($R=0.96$, $p=0.0006$). ctHHb ($R=0.96$, $p=0.001$) and lipids ($R=-0.85$, $p=0.03$) also were correlated with SBR but to a lesser degree, generally due to higher variations. Note that the
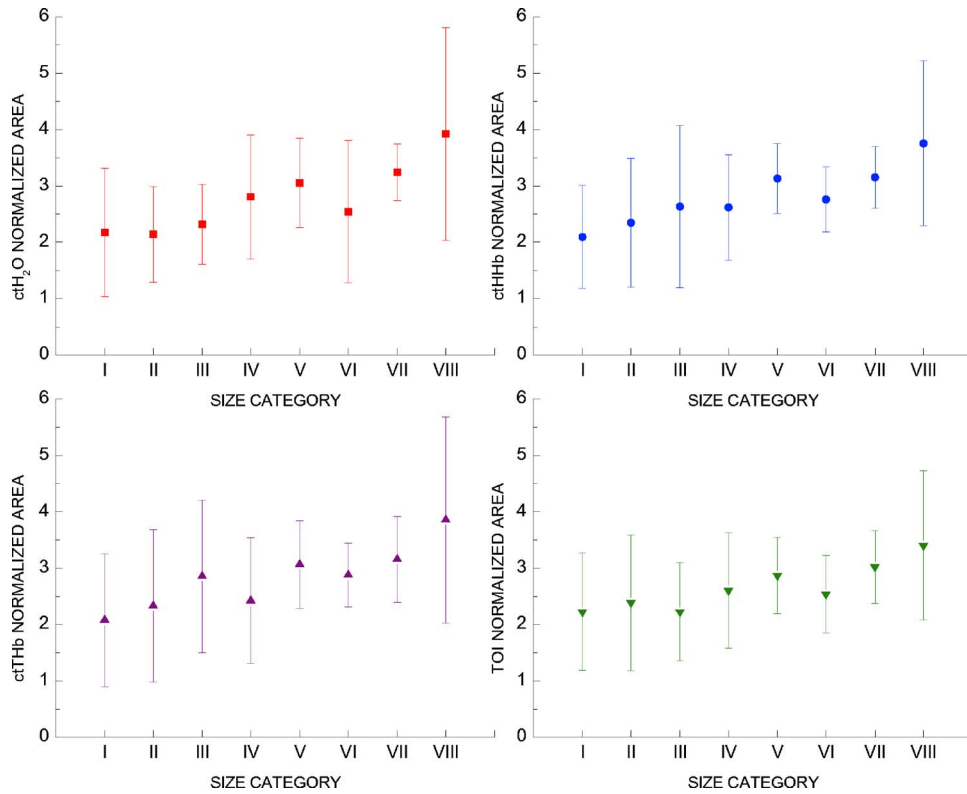
Fig. 9 Plots of normalized tumor area versus size category. Normalized tumor area was determined by integrating DOS parameters over the tumor locations in a normalized linescan. Although there is high variation, there is a weak general trend in size. Error bars represent the standard deviation for each parameter for all subjects within a given size category.

lipid signal decreased with increasing SBR, but this effect is likely due to the fact that the lesion size tended to increase with increasing SBR. The correlation between SP and SBR was lower ($R=-0.61$) and not significant ($p=0.2$). Note that the SBR=4 point was also excluded from these error-weighted fits since there was only a single subject with SBR=4.

4 Discussion

4.1 *General Remarks*

Broadband DOS measurements display enormous spectral sensitivity at the expense of spatial resolution. Since the tumor locations were known *a priori*, the low degree of spatial sampling by our technique was not a serious limitation. Measured tumor spectra likely contained contributions from both normal and diseased tissues, the balance of which varied with lesion size and depth, as well as the optical properties of the tissues within the field of view. Image reconstructions would

be able to isolate the optical properties of tumor and normal tissues better than the simple scheme we have presented here. In some cases, true contrast can be higher than we have presented, although many of our stage III tumors were large enough to occupy a sizable field of view within the probe. Because the biological processes that determine the origins of optical contrast are conserved across spatial scales, intrinsic optical signals measured from these subjects are expected to be similar for earlier stage invasive cancers.

4.2 *Significance of Absorption Contrast*

Changes in ctHHb were the most significant of all the base parameters. We found that ctHHb generally produced the largest relative changes in the average (48%) and peak (68%) linescan values. Although ctHHb is the most sensitive parameter, additional tissue constituents such as water and lipid also produced significant differences that could aid in the detection and characterization of breast lesions. For the peak tumor val-

Table 6 Size categories.

	I	II	III	IV	V	VI	VII	VIII
MIN SIZE (mm)		$10\geqslant$	$15\geqslant$	$20\geqslant$	$25\geqslant$	$30\geqslant$	$40\geqslant$	$60\geqslant$
MAX SIZE (mm)	<10	<15	<20	<25	<30	<40	60	NA
N	5	7	6	4	6	7	4	7
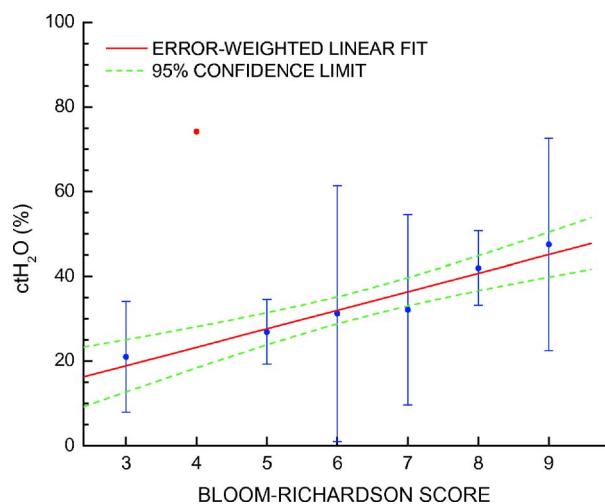
Fig. 10 Peak tumor water concentration versus Bloom—Richardson score. Each score is represented by the average of all of the data. The solid line is an error-weighted fit of all of the points, except for the point at a Bloom—Richardson score of 4. Only 37 of the 58 tumors received Bloom—Richardson scores.

ues, we observed changes in absolute percent for lipids and water to be >13% for each parameter.

Surprisingly, the stO_2 was the least sensitive figure of merit presented here. In particular, the average value of the stO_2 linescan was not significantly different than the normal linescan. The stO_2 has been commonly used as a figure of merit for breast cancer detection. According to our results, the hemoglobin concentrations themselves were far better indices for cancer detection. Even the minimum stO_2-value of the tumor linescans averaged for all subjects was about 61%. There were patients where the stO_2 dropped significantly, as one might expect, but this was not always the case. Typically we have seen large stO_2 decreases in large necrotic tumors; a good example of this may be found in a detailed recent publication.[20] The hemoglobin concentration in the breast is relatively low, especially in the post-menopausal breast, so that small errors in concentration manifest as large errors in stO_2. This error will only be amplified by ignoring the contribution of water and lipids.[30]

We also observe that there is important contrast between normal and malignant available in the 900+ nm range (water and lipids). The extra information here may be important, although few optical mammography studies have taken advantage of the information content offered by this spectral region. Water and lipid contrast may aid in lesion detection, as evidenced by the usefulness of the TOI. As breast tumors grow, they begin to push away adipose tissue. In addition, the water may be an index of cellularity, and may thus report on the aggressiveness of the tumor.[52–54] Significant changes in water and lipids resulting from neoadjuvant chemotherapy have also been observed in DOS[19] as well as MRI.[78] Finally, water and lipid content play a role in mammographic density, which is correlated to breast cancer risk.[79,80]

4.3 *Significance of Scattering Contrast*

We observed significant changes not only in absorption-derived parameters, but also in reduced scattering-derived pa-

rameters. Both SP and A exhibited high variance. Nevertheless, we observed that both the tumor peak and average exhibit a higher SP and A than the surrounding regions of "normal" tissue on the tumor side as well as the contralateral breast side.

The dependence of the A as a function of SP was different for each measurement class; N_{AVG}, T_{BASE}, and T_{MAX}. We found that within the errors [log(A) versus SP]; T_{MAX} revealed the lowest slope. Since A is related to the density of scattering centers, and SP is related to the size of the scattering centers relative to the optical wavelength, we see that as tissues become cancerous, the balance between scatter density and size changes. That scatter density and/ or scatter size could change during malignant transformation is not surprising. For example, it is known that the nuclear/cytoplasmic ratio is greater in cancer cells relative to normal cells. Tissue cellularity, or cell density, is also known to increase in cancerous tissues relative to their normal counterparts. Our result suggests that there is a coupling between these size and density parameters as measured in heterogeneous breast tissues. The effect could be due to limitations in the diffusion model that arise by application to heterogeneous tissues. A more detailed analysis of tissue scattering parameters, and how these parameters change during malignant transformation, merits further investigation.

Past efforts have shown that as SP increases, the average scatterer size decreases.[33,68] In particular, the work of Mourant et al. has demonstrated that tumorgenic cell suspensions have a lower SP and a higher A than normal cell suspensions.[33] Our results would seem at first to contradict these findings. However, we note that breast carcinomas such as those studied here have a glandular origin. These glandular tissues have a higher collagen content and a higher scatter power than tissues with less collagen content, such as adipose.[30] Thus, the scattering changes observed here may be more reflective of extracellular matrix fibrosis or diminished adipose than intracellular structure.

4.4 *Comments on Spatial Heterogeneity*

We have noted that all of the DOS-derived functional information did not peak or trough at the exact same position along the linescan. It is most likely that these effects are due to the low-spatial sampling frequency we have adopted here. The tumor depth below the surface will change with position so that each linescan point samples different combinations of tumor and normal tissue. In addition, since tumors are heterogeneous structures, each of the tumor regions themselves will also vary with spatial location. Thus, it is not surprising that we have observed variability in the minima and maxima of the DOS parameters. By introducing functional indices that take advantage of all of the optical contrast available, one can convolve this information into a single parameter (e.g., tissue optical index, TOI) that can be reflective of various functional changes in cellular metabolism, extracellular matrix composition, and angiogenesis that are consistent with malignant tumor physiology.

4.5 *Comments on Tumor Size*

We did not see any correlations between the tumor peak values and tumor size. However, there was a weak correlation

between the spatial extent of the DOS parameters and tumor size. The ctH$_2$O spatial extent signal correlated best with tumor size. These observations must be balanced with the fact that we did not take into account the lesion orientation. We note that a two-layer model of the breast will be necessary to strengthen this observation, since the presence of lipids in an adipose layer above the tumor will affect the spatial extent of the DOS linescan. In our limited-spatial sampling reflectance geometry, we are likely only probing the top regions of deeper or larger lesions. Efforts to construct a handpiece with depth-sectioning capabilities are currently underway.

Almost 20% of the lesions studied (11/58) were below 15 mm in their largest axis. About 12% (7/58) were below 10 mm, with a low of 5 mm. These relatively small lesions were still measurable within this idealized nonscreening sample, despite both low-spatial sampling and inherent resolution limitations of diffuse optics. Since we do not have depth information for these lesions, we can only speculate as to the reason for the detectable contrast within this sample. We believe this is a direct result of the fact that the tumor perturbs a region of tissue that is larger than the tumor itself. Inflammation, fibrosis, and increased blood flow all occur on a spatial scale larger than the cancer cells, thus amplifying our sensitivity. Measuring and classifying lesions this small in a screening study would, of course, be much more difficult.

4.6 Comments on Tissue Water

Figure 10 provides preliminary evidence of a link between the microscopic environment of cancer cells and the macroscopically measured tissue optical properties. Higher SBR scores are associated with (1) lower microtubule formation, (2) increasingly varied nuclear pleomorphism, and (3) increased mitosis.[81] SBR scores are associated with prognosis; patients with smaller scores have significantly better survival than patients with higher scores.[81] SBR may also be a predictor of tumor response to neoadjuvant chemotherapy.[82]

DOS-measured water content correlates with SBR (and tumor size) most likely because tissue water is related to tissue cellularity. Highly cellular tissues, such as cancer, have impeded diffusion, as evidenced by diffusion-weighted MRI.[57] Impeded diffusion implies an increase in ctH$_2$O, which we have observed consistently in our studies. Thus, the degree of cellular density is linked to the SBR score through ctH$_2$O. We recognize that this result is somewhat speculative given the high degree of variation in the data. We plan to confirm this result using preclinical animal models, where the SBR scores, cellularity, and ctH$_2$O can be systematically controlled.

5 Conclusions

We have presented quantitative, *in vivo* measurements of intrinsic optical contrast between malignant and normal breast tissues in 58 subjects. The functional origins of this contrast depend strongly upon the age of the subject and include both hemodynamic (ctHHb and ctO$_2$Hb) and parenchymal (ctH$_2$O and lipid) components. Although tissue scatter power and scatter amplitude are highly coupled, we found that the relationship between them changes as tissues progress from normal to cancerous. We also found a link between the microscopic histological grading scale (Scarff–Bloom–Richardson) and ctH$_2$O. These high spectral content broadband diffuse

optical spectroscopy (DOS) measurements provide a multidimensional view of tissue function and composition. Ultimately, we expect these data will play an important role in enhancing the performance and design of clinical optical mammography techniques.

References

1. D. S. Buist, P. L. Porter, C. Lehman, S. H. Taplin, and E. White, "Factors contributing to mammography failure in women aged 40–49 years," *J. Natl. Cancer Inst.* **96**, 1432–1440 (2004).
2. K. Kerlikowske, J. Barclay, D. Grady, E. A. Sickles, and V. Ernster, "Comparison of risk factors for ductal carcinoma in situ and invasive breast cancer," *J. Natl. Cancer Inst.* **89**, 76–82 (1997).
3. M. J. Homer, "Breast imaging: Pitfalls, controversies, and some practical thoughts," *Radiol. Clin. North Am.* **23**, 459–472 (1985).
4. J. G. Elmore, M. B. Barton, V. M. Moceri, S. Polk, P. J. Arena, and S. W. Fletcher, "Ten-year risk of false positive screening mammograms and clinical breast examinations," *N. Engl. J. Med.* **338**, 1089–1096 (1998).
5. P. A. Carney, D. L. Miglioretti, B. C. Yankaskas, K. Kerlikowske, R. Rosenberg, C. M. Rutter, B. M. Geller, L. A. Abraham, S. H. Taplin, M. Dignan, G. Cutter, and R. Ballard-Barbash, "Individual and combined effects of age, breast density, and hormone replacement therapy use on the accuracy of screening mammography," *Ann. Intern Med.* **138**, 168–175 (2003).
6. E. D. Pisano, C. Gatsonis, E. Hendrick, M. Yaffe, J. K. Baum, S. Acharyya, E. F. Conant, L. L. Fajardo, L. Bassett, C. D'Orsi, R. Jong, and M. Rebner, "Diagnostic performance of digital versus film mammography for breast-cancer screening," *N. Engl. J. Med.* **353**, 1773–1783 (2005).
7. M. C. Segel, D. D. Paulus, and G. N. Hortobagyi, "Advanced primary breast cancer: Assessment at mammography of response to induction chemotherapy," *Radiology* **169**, 49–54 (1988).
8. E. C. Moskovic, J. L. Mansi, D. M. King, C. R. Murch, and I. E. Smith, "Mammography in the assessment of response to medical treatment of large primary breast cancer," *Clin. Radiol.* **47**, 339–344 (1993).
9. M. A. Helvie, L. K. Joynt, R. L. Cody, L. J. Pierce, D. D. Adler, and S. D. Merajver, "Locally advanced breast carcinoma: accuracy of mammography versus clinical examination in the prediction of residual disease after chemotherapy," *Radiology* **198**, 327–332 (1996).
10. S. Huber, M. Wagner, I. Zuna, M. Medl, H. Czembirek, and S. Delorme, "Locally advanced breast carcinoma: Evaluation of mammography in the prediction of residual disease after induction chemotherapy," *Anticancer Res.* **20**, 553–558 (2000).
11. L. D. Feldman, G. N. Hortobagyi, A. U. Buzdar, F. C. Ames, and G. R. Blumenschein, "Pathological assessment of response to induction chemotherapy in breast cancer," *Cancer Res.* **46**, 2578–2581 (1986).
12. M. R. Machiavelli, A. O. Romero, J. E. Perez, J. A. Lacava, M. E. Dominguez, R. Rodriguez, M. R. Barbieri, L. A. Romero Acuna, J. M. Romero Acuna, M. J. Langhi, S. Amato, E. H. Ortiz, C. T. Vallejo, and B. A. Leone, "Prognostic significance of pathological response of primary tumor and metastatic axillary lymph nodes after neoadjuvant chemotherapy for locally advanced breast carcinoma," *Cancer J. Sci. Am.* **4**, 125–131 (1998).

13. S. J. Vinnicombe, A. D. MacVicar, R. L. Guy, J. P. Sloane, T. J. Powles, G. Knee, and J. E. Husband, "Primary breast cancer: Mammographic changes after neoadjuvant chemotherapy, with pathologic correlation," *Radiology* **198**, 333–340 (1996).
14. S. Fantini, S. A. Walker, M. A. Franceschini, M. Kaschke, P. M. Schlag, and K. T. Moesta, "Assessment of the size, position, and optical properties of breast tumors *in vivo* by noninvasive optical methods," *Appl. Opt.* **37**, 1982–1989 (1998).
15. M. A. Franceschini, K. T. Moesta, S. Fantini, G. Gaida, E. Gratton, H. Jess, W. W. Mantulin, M. Seeber, P. M. Schlag, and M. Kaschke, "Frequency-domain techniques enhance optical mammography: Initial clinical results," *Proc. Natl. Acad. Sci. U.S.A.* **94**, 6468–6473 (1997).
16. B. J. Tromberg, O. Coquoz, J. B. Fishkin, T. Phan, E. R. Anderson, J. Butler, M. Cahn, J. D. Gross, V. Venugopalan, and D. Pham, "Non-invasive measurements of breast tissue optical properties using frequency-domain photon migration," *Philos. Trans. R. Soc. London, Ser. B* **352**, 661–668 (1997).
17. B. J. Tromberg, N. Shah, R. Lanning, A. Cerussi, J. Espinoza, T. Pham, L. Svaasand, and J. Butler, "Non-invasive *in vivo* characterization of breast tumors using photon migration spectroscopy," *Neoplasia* **2**, 26–40 (2000).
18. B. W. Pogue, S. P. Poplack, T. O. McBride, W. A. Wells, K. S. Osterman, U. L. Osterberg, and K. D. Paulsen, "Quantitative hemoglobin tomography with diffuse nearinfrared spectroscopy: Pilot results in the breast," *Radiology* **218**, 261–266 (2001).
19. D. B. Jakubowski, A. E. Cerussi, F. Bevilacqua, N. Shah, D. Hsiang, J. Butler, and B. J. Tromberg, "Monitoring neoadjuvant chemotherapy in breast cancer using quantitative diffuse optical spectroscopy: A case study," *J. Biomed. Opt.* **9**, 230–238 (2004).
20. N. Shah, J. Gibbs, D. Wolverton, A. Cerussi, N. Hylton, and B. Tromberg, "Combined diffuse optical spectroscopy and contrast-enhanced MRI for monitoring breast cancer neoadjuvant chemotherapy: A case study," *J. Biomed. Opt.* **10**, 051503 (2005).
21. Q. Zhu, S. H. Kurtzma, P. Hegde, S. Tannenbaum, M. Kane, M. Huang, N. G. Chen, B. Jagjivan, and K. Zarfos, "Utilizing optical tomography with ultrasound localization to image heterogeneous hemoglobin distribution in large breast cancers," *Neoplasia* **7**, 263–270 (2005).
22. R. Choe, A. Corlu, K. Lee, T. Durduran, S. D. Konecky, M. Grosicka-Koptyra, S. R. Arridge, B. J. Czerniecki, D. L. Fraker, A. DeMichele, B. Chance, M. A. Rosen, and A. G. Yodh, "Diffuse optical tomography of breast cancer during neoadjuvant chemotherapy: A case study with comparison to MRI," *Med. Phys.* **32**, 1128–1139 (2005).
23. S. Srinivasan, B. W. Pogue, S. Jiang, H. Dehghani, C. Kogel, S. Soho, J. J. Gibson, T. D. Tosteson, S. P. Poplack, and K. D. Paulsen, "Interpreting hemoglobin and water concentration, oxygen saturation, and scattering measured *in vivo* by near-infrared breast tomography," *Proc. Natl. Acad. Sci. U.S.A.* **100**, 12349–12354 (2003).
24. B. C. Wilson, M. S. Patterson, S. T. Flock, and D. R. Wyman, "Tissue optical properties in relation to light propagation models and *in vivo* dosimetry," in *Photon Migration in Tissues*, B. Chance, ed. Plenum, New York, 1988, 25–42.
25. M. Cope, "The application of near infrared spectroscopy to non invasive monitoring of cerebral oxygenation in the newborn infant," in *Dept. Med. Phys. Bioeng.* University College of London (1991).
26. E. M. Sevick, B. Change, J. Leigh, S. Nioka, and M. Maris, "Quantitation of time-resolved and frequency-resolved optical spectra for the determination of tissue oxygenation," *Anal. Biochem.* **195**, 330–351 (1991).
27. J. R. Mourant, M. Canpolat, C. Brocker, O. Esponda-Ramos, T. M. Johnson, A. Matanock, K. Stetter, and J. P. Freyer, "Light scattering from cells: The contribution of the nucleus and the effects of proliferative status," *J. Biomed. Opt.* **5**, 131–137 (2000).
28. S. L. Jacques, "Origins of tissue optical properties in the UVA, visible, and NIR regions," 1996.
29. B. Beauvoit and B. Chance, "Time-resolved spectroscopy of mitochondria, cells and tissues under normal and pathological conditions," *Mol. Cell. Biochem.* **184**, 445–455 (1998).
30. A. E. Cerussi, D. Jakubowski, N. Shah, F. Bevilacqua, R. Lanning, A. J. Berger, D. Hsiang, J. Butler, R. F. Holcombe, and B. J. Tromberg, "Spectroscopy enhances the information content of optical mammography," *J. Biomed. Opt.* **7**, 60–71 (2002).
31. B. W. Pogue, S. Jiang, H. Dehghani, C. Kogel, S. Soho, S. Srinivasan, X. Song, T. D. Tosteson, S. P. Poplack, and K. D. Paulsen, "Characterization of hemoglobin, water, and NIR scattering in breast tissue: Analysis of intersubject variability and menstrual cycle changes," *J. Biomed. Opt.* **9**, 541–552 (2004).
32. L. Spinelli, A. Torricelli, A. Pifferi, P. Taroni, G. M. Danesini, and R. Cubeddu, "Bulk optical properties and tissue components in the female breast from multiwavelength time-resolved optical mammography," *J. Biomed. Opt.* **9**, 1137–1143 (2004).
33. J. R. Mourant, A. H. Hielscher, A. A. Eick, T. M. Johnson, and J. P. Freyer, "Evidence of intrinsic differences in the light scattering properties of tumorigenic and nontumorigenic cells," *Cancer (N.Y.)* **84**, 366–374 (1998).
34. D. Jakubowski, "Development of broadband quantitative tissue optical spectroscopy for the non-invasive characterization of breast disease," in *Physics*, University of California, Irvine (2002).
35. F. Bevilacqua, A. J. Berger, A. E. Cerussi, D. Jakubowski, and B. J. Tromberg, "Broadband absorption spectroscopy in turbid media by combined frequency-domain and steady-state methods," *Appl. Opt.* **39**, 6498–6507 (2000).
36. S. Ertefai and A. E. Profio, "Spectral transmittance and contrast in breast diaphanography," *Med. Phys.* **12**, 393–400 (1985).
37. V. Quaresima, S. J. Matcher, and M. Ferrari, "Identification and quantification of intrinsic optical contrast for near-infrared mammography," *Photochem. Photobiol.* **67**, 4–14 (1998).
38. R. Cubeddu, C. D'Andrea, A. Pifferi, P. Taroni, A. Torricelli, and G. Valentini, "Effects of the menstrual cycle on the red and near-infrared optical properties of the human breast," *Photochem. Photobiol.* **72**, 383–391 (2000).
39. N. Shah, A. E. Cerussi, D. Jakubowski, D. Hsiang, J. Butler, and B. J. Tromberg, "The role of diffuse optical spectroscopy in the clinical management of breast cancer," *Dis. Markers* **19**, 95–105 (2003).
40. A. Pifferi, P. Taroni, A. Torricelli, F. Messina, R. Cubeddu, and G. Danesini, "Fourwavelength time-resolved optical mammography in the 680–980-nm range," *Opt. Lett.* **28**, 1138–1140 (2003).
41. R. Zander and F. Mertzlufft, "Tentative recommendations on terminology and definitions in the respiratory physiology: Resume of the ISOTT consensus session 1992," *Adv. Exp. Med. Biol.* **345**, 913–919 (1994).
42. D. Grosenick, H. Wabnitz, H. H. Rinneberg, K. T. Moesta, and P. M. Schlag, "Development of a time-domain optical mammograph and first *in vivo* applications," *Appl. Opt.* **38**, 2927–2943 (1999).
43. Q. Zhu, E. Conant, and B. Chance, "Optical imaging as an adjunct to sonograph in differentiating benign from malignant breast lesions," *J. Biomed. Opt.* **5**, 229–236 (2000).
44. M. A. Franceschini, S. Fantini, A. Cerussi, B. Barbieri, B. Chance, and E. Gratton, "Quantitative spectroscopic determination of hemoglobin concentration and saturation in a turbid medium: Analysis of the effect of water absorption," *J. Biomed. Opt.* **2**, 147–153 (1997).
45. E. L. Hull, M. G. Nichols, and T. H. Foster, "Quantitative broadband near-infrared spectroscopy of tissue-simulating phantoms containing erythrocytes," *Phys. Med. Biol.* **43**, 3381–3404 (1998).
46. G. Strangman, M. A. Franceschini, and D. A. Boas, "Factors affecting the accuracy of near-infrared spectroscopy concentration calculations for focal changes in oxygenation parameters," *Neuroimage* **18**, 865–879 (2003).
47. E. L. Heffer and S. Fantini, "Quantitative oximetry of breast tumors: A near-infrared method that identifies two optimal wavelengths for each tumor," *Appl. Opt.* **41**, 3827–3839 (2002).
48. T. Sugahara, Y. Korogi, M. Kochi, I. Ikushima, Y. Shigematu, T. Hirai, T. Okuda, L. Liang, Y. Ge, Y. Komohara, Y. Ushio, and M. Takahashi, "Usefulness of diffusion-weighted MRI with echo-planar technique in the evaluation of cellularity in gliomas," *J. Magn. Reson Imaging* **9**, 53–60 1999.
49. C. G. Filippi, M. A. Edgar, A. M. Ulug, J. C. Prowda, L. A. Heier, and R. D. Zimmerman, "Appearance of meningiomas on diffusion-weighted images: correlating diffusion constants with histopathologic findings," *AJNR Am. J. Neuroradiol.* **22**, 65–72 (2001).
50. K. Kono, Y. Inoue, K. Nakayama, M. Shakudo, M. Morino, K. Ohata, K. Wakasa, and R. Yamada, "The role of diffusion-weighted imaging in patients with brain tumors," *AJNR Am. J. Neuroradiol.* **22**, 1081–1088 (2001).
51. H. Rumpel, J. B. Khoo, H. M. Chang, W. E. Lim, C. Chen, M. C. Wong, and K. P. Tan, "Correlation of the apparent diffusion coefficient and the creatine level in early ischemic stroke: A comparison of

different patterns by magnetic resonance," *J. Magn. Reson Imaging* **13**, 335–343 (2001).

52. Y. Guo, Y. Q. Cai, Z. L. Cai, Y. G. Gao, N. Y. An, L. Ma, S. Mahankali, and J. H. Gao, "Differentiation of clinically benign and malignant breast lesions using diffusion-weighted imaging," *J. Magn. Reson Imaging* **16**, 172–178 (2002).

53. S. Sinha, F. A. Lucas-Quesada, U. Sinha, N. DeBruhl, and L. W. Bassett, "*In vivo* diffusion-weighted MRI of the breast: potential for lesion characterization," *J. Magn. Reson Imaging* **15**, 693–704 (2002).

54. M. A. Thomas, N. Wyckoff, K. Yue, N. Binesh, S. Banakar, H. K. Chung, J. Sayre, and N. DeBruhl, Two-dimensional MR spectroscopic characterization of breast cancer *in vivo*, *Technol. Cancer Res. Treat.* **4**, 99–106 (2005).

55. Y. Nonomura, M. Yasumoto, R. Yoshimura, K. Haraguchi, S. Ito, T. Akashi, and I. Ohashi, "Relationship between bone marrow cellularity and apparent diffusion coefficient," *J. Magn. Reson Imaging* **13**, 757–760 (2001).

56. A. Baur, O. Dietrich, and M. Reiser, "Diffusion-weighted imaging of bone marrow: current status," *Eur. Radiol.* **13**, 1699–1708 (2003).

57. H. Lyng, O. Haraldseth, and E. K. Rofstad, "Measurement of cell density and necrotic fraction in human melanoma xenografts by diffusion weighted magnetic resonance imaging," *Magn. Reson. Med.* **43**, 828–836 (2000).

58. Y. Paran, P. Bendel, R. Margalit, and H. Degani, "Water diffusion in the different microenvironments of breast cancer," *NMR Biomed.* **17**, 170–180 (2004).

59. H. A. Rowley, P. E. Grant, and T. P. Roberts, *Diffusion MR imaging. Theory and applications*, *Neuroimaging Clin. N. Am.* **9**, 343–361 (1999).

60. S. Merritt, G. Gulsen, G. Chiou, Y. Chu, C. Deng, A. E. Cerussi, A. J. Durkin, B. J. Tromberg, and O. Nalcioglu, "Comparison of water and lipid content measurements using diffuse optical spectroscopy and MRI in emulsion phantoms," *Technol. Cancer Res. Treat.* **2**, 563–569 (2003).

61. B. Brooksby, S. Jiang, H. Dehghani, B. Pogue, C. Paulsen, C. Kogel, M. Doyley, J. Weaver, and S. Poplack, "Magnetic resonance-guided near-infrared tomography of the breast," *Rev. Sci. Instrum.* **75**, 5262–5270 (2004).

62. J. B. Fishkin and E. Gratton, "Propagation of photon-density waves in strongly scattering media containing an absorbing semi-infinite plane bounded by a straight edge," *J. Opt. Soc. Am. A* **10**, 127–140 (1993).

63. L. O. Svaasand, B. J. Tromberg, R. C. Haskell, T. Tsong-Tseh, and M. W. Berns, "Tissue characterization and imaging using photon density waves," *Opt. Eng.* **32**, 258–266 (1993).

64. J. B. Fishkin, S. Fantini, M. J. vandeVen, and E. Gratton, "Gigahertz photon density waves in a turbid medium: Theory and experiments," *Phys. Rev. E* **53**, 2307–2319 (1996).

65. R. C. Haskell, L. O. Svaasand, T. Tsong-Tseh, F. Ti-Chen, M. S. McAdams, and B. J. Tromberg, "Boundary conditions for the diffusion equation in radiative transfer," *J. Opt. Soc. Am. A* **11**, 2727–2741 (1994).

66. T. H. Pham, O. Coquoz, J. B. Fishkin, E. Anderson, and B. J. Tromberg, "Broad bandwidth frequency domain instrument for quantitative tissue optical spectroscopy," *Rev. Sci. Instrum.* **71**, 2500–2513 (2000).

67. J. R. Mourant, T. Fuselier, J. Boyer, T. M. Johnson, and I. J. Bigio, "Predictions and measurements of scattering and absorption over

broad wavelength ranges in tissue phantoms," *Appl. Opt.* **36**, 949–957 (1997).

68. A. M. K. Nilsson, C. Sturesson, D. L. Liu, and S. Andersson-Engels, "Changes in spectral shape of tissue optical properties in conjunction with laser-induced thermotherapy," *Appl. Opt.* **37**, 1256–1267 (1998).

69. A. Kienle and M. S. Patterson, "Improved solutions of the steady-state and the timeresolved diffusion equations for reflectance from a semi-infinite turbid medium," *J. Opt. Soc. Am. A* **14**, 246–254 (1997).

70. L. Kou, D. Labrie, and P. Chylek, "Refractive indices of water and ice in the 0.65- to 2.5-μm spectral range," *Appl. Opt.* **32**, 3531–3540 (1993).

71. C. Eker, "Optical characterization of tissue for medical diagnostics," in *Dept. of Physics*, Lund Institute of Technology, Lund (1999).

72. W. G. Zijlstra, A. Buursma, and O. W. V. Assendelft, *Visible and Near Infrared Absorption Spectra of Human and Animal Haemoglobin: Determination and Application*: VSP, 2000.

73. P. Taroni, G. Danesini, A. Torricelli, A. Pifferi, L. Spinelli, and R. Cubeddu, "Clinical trial of time-resolved scanning optical mammography at 4 wavelengths between 683 and 975 nm," *J. Biomed. Opt.* **9**, 464–473 (2004).

74. P. Taroni, A. Pifferi, A. Torricelli, D. Comelli, and R. Cubeddu, "*In vivo* absorption and scattering spectroscopy of biological tissues," *Photochem. Photobiol.* **2**, 124–129 (2003).

75. T. Durduran, R. Choe, J. P. Culver, L. Zubkov, M. J. Holboke, J. Giammarco, B. Chance, and A. G. Yodh, "Bulk optical properties of healthy female breast tissue," *Phys. Med. Biol.* **47**, 2847–2861 (2002).

76. 6H. J. Bloom and W. W. Richardson, "Histological grading and prognosis in breast cancer; a study of 1409 cases of which 359 have been followed for 15 years," *Br. J. Cancer* **11**, 359–377 (1957).

77. V. Le Doussal, M. Tubiana-Hulin, S. Friedman, K. Hacene, F. Spyratos, and M. Brunet, "Prognostic value of histologic grade nuclear components of Scarff-Bloom-Richardson (SBR). An improved score modification based on a multivariate analysis of 1262 invasive ductal breast carcinomas," *Cancer* **64**, 1914–1921 (1989).

78. N. R. Jagannathan, M. Singh, V. Govindaraju, P. Raghunathan, O. Coshic, P. K. Julka, and G. K. Rath, "Volume localized *in vivo* proton MR spectroscopy of breast carcinoma: Variation of water-fat ratio in patients receiving chemotherapy," *NMR Biomed.* **11**, 414–422 (1998).

79. A. F. Saftlas, R. N. Hoover, L. A. Brinton, M. Szklo, D. R. Olson, M. Salane, and J. N. Wolfe, "Mammographic densities and risk of breast cancer," *Cancer* **67**, 2833–2838 (1991).

80. J. J. Heine and P. Malhotra, "Mammographic tissue, breast cancer risk, serial image analysis, and digital mammography. Part 1. Tissue and related risk factors," *Acad. Radiol.* **9**, 298–316 (2002).

81. C. W. Elston and I. O. Ellis, "Pathological prognostic factors in breast cancer. I. The value of histological grade in breast cancer: Experience from a large study with long-term follow-up," *Histopathology* **19**, 403–410 (1991).

82. S. Amat, F. Penault-Llorca, H. Cure, G. Le Bouedec, J. L. Achard, I. Van Praagh, V. Feillel, M. A. Mouret-Reynier, J. Dauplat, and P. Chollet, "Scarff-Bloom-Richardson (SBR) grading: A pleiotropic marker of chemosensitivity in invasive ductal breast carcinomas treated by neoadjuvant chemotherapy," *Int. J. Oncol.* **20**, 791–796 (2002).